International Journal of Extreme Manufacturing

Material embrittlement in high strain-rate loading

OPEN ACCESS
IOP Publishing | IMMT
International Journal of Extreme Manufacturing
Int. J. Extrem. Manuf. 1 (2019) 022003 (19pp)
https://doi.org/10.1088/2631-7990/ab263f

Topical Review

Material embrittlement in high strain-rate loading

Xiuxuan Yang[1] **and Bi Zhang**[2,3,4]

[1] Dalian University of Technology, Dalian, People's Republic of China
[2] The Southern University of Science and Technology, Shenzhen, People's Republic of China
[3] The University of Connecticut, Storrs, CT, United States of America

E-mail: yangxiuxuan@mail.dlut.edu.cn, Zhangb@SUSTech.edu.cn and bi.zhang@uconn.edu

Received 1 April 2019, revised 17 May 2019
Accepted for publication 17 May 2019
Published 21 June 2019

Abstract

Material embrittlement is often encountered in machining, heat treatment, hydrogen and low-temperature conditions among which machining is strain-rate related. More strain-rate evoked embrittlement is expected in material loading processes, such as in high-speed machining and projectile penetration. In order to understand the fundamental mechanisms of the strain-rate evoked material embrittlement, this study is concerned with the material responses to loading at high strain-rates. It then explores the strain-rate evoked material embrittlement and fragmentation during high strain-rate loading processes and evaluates various empirical and physical models from different researchers for the assessment of the material embrittlement. The study proposes strain-rate sensitivity for the characterization of material embrittlement and the concept of the pseudo embrittlement for material responses to very high strain-rates. A discussion section is arranged to explore the underlying mechanisms of the strain-rate evoked material embrittlement and fragmentation based on dislocation kinetics.

Keywords: embrittlement, strain rate, strain-rate sensitivity, dislocation

(Some figures may appear in colour only in the online journal)

1. Introduction

Material embrittlement can be due to different causes. Tensile stress triaxiality, heat treatment, and low-temperature conditions, for example, are the causes that can lead to material embrittlement. Table 1 lists the common types of material embrittlement among which high-speed machining is often encountered and characterized by high strain-rate loading. Welding embrittlement is related to material segregation and precipitation. The formation of the 'Cottrell atmosphere' during a welding process impedes dislocation movement and causes precipitation embrittlement [1]. In addition, in a heat treatment process of steel, the blue embrittlement may occur at a certain temperature as dislocations are hindered by the carbon and nitrogen atoms, which leads to an increase in strength of a material [2]. Low-temperature embrittlement is due to the increase in the critical stress for the dislocation movement [3, 4]. Hydrogen embrittlement is a result of the decrease in surface energy caused by the generation of hydride or the attachment of hydrogen atoms to crack tips if any [5]. Irradiation embrittlement is common in nuclear containers, as the point defects generated by the irradiation interact with the solute atoms to form precipitates, hindering dislocation movements and resulting in material embrittlement [6–8].

Material embrittlement can be a result of an enhanced strength and hardness, and a reduced fracture toughness of a material. In fact, material embrittlement occurs in the

[4] Author to whom any correspondence should be addressed.

Table 1. Common types of embrittlement.

Condition	Embrittlement cause
Process related	(a) Welding
	(b) Heat treatment
	(c) High strain-rate loading
	(d) Triaxial tensile stress loading
Environment related	(a) Hydrogen
	(b) Irradiation
	(c) Corrosion
	(d) Low-temperature

processes of, for example, machining, projectile penetration, explosion, and tunnel boring, because of the high strain-rates in the processes, as specified in table 2. Many researchers also suggested that a high strain-rate should lead to material embrittlement. Chilton *et al* [9] investigated the ductile-to-brittle transition of tungsten at low temperatures, and found the ductile-to-brittle transition temperature of the material increased with strain rate.

In a machining process, strain rate can reach up to $10^7\ s^{-1}$ at which embrittlement should occur in many materials [10]. Material embrittlement at high strain-rates paves a practical way towards machining of difficult-to-machine materials with high efficiency and high quality. The problems (e.g. built-up edges and wheel loading) that are constantly associated with the conventional machining processes may no longer exist in a high-speed machining process as a material can be temporarily embrittled for improved machinability during such a process.

The difficult-to-machine materials (hard and brittle materials, composites, titanium alloys, nickel alloys, etc) generally have outstanding mechanical and physical properties and are widely used in the aerospace and defense, semiconductor, automotive, and cutting tool industries [24–26]. However, these materials are difficult-to-machine because they often create machining problems, such as surface and subsurface damage to the workpiece, poor workpiece surface finish and dimensional accuracies, chatter and vibrations in a machining process, and cutting tool wear. Many researchers recognize that high-speed machining is an effective method to solve the machining problem of the difficult-to-machine materials and is helpful in improving machining efficiency and surface quality, and suppressing subsurface damage [27–29]. Studies also reported that material embrittlement in the grinding processes helped reduce subsurface damage depth [30, 31]. Material embrittlement can be induced at a high strain-rate that is realized in a high-speed machining process. It is expected to solve the typical problems involved in the conventional machining processes, such as built-up edges, grinding wheel loading, workpiece burn, burr formation, surface chipping, and surface integrity (e.g. cracking, residual stresses, plastic deformation, and phase transformation). Unfortunately, the strain-rate evoked material embrittlement is not fully understood, and its fundamental mechanisms are to be investigated [32].

This study is focused on the material embrittlement mechanisms of the engineering materials subjected to loading at high strain-rates. Section 2 describes material responses to loading at high strain-rates; sections 3 is related to material embrittlement at high strain-rates; section 4 provides discussion on the strain-rate evoked material embrittlement; and section 5 summarizes the paper and draws conclusions.

2. Material responses to loading at high strain-rates

To understand the embrittlement mechanisms under the high strain-rate conditions, it is necessary to study material responses to loadings under such conditions. Generally, experimental methods and constitutive models are established for studying the material responses to mechanical loadings, which is presented in this section.

2.1. High strain-rate loading processes

Material responses to loading at high strain-rates can be experimentally investigated and analyzed. One of the widely used techniques is the split Hopkinson pressure bar (SHPB) that consists of a striker and the incident and transmission bars between which a specimen is placed in. Figure 1 shows the schematic diagram of SHPB for studying the mechanical properties of a specimen at high strain-rates. SHPB is widely used for both ductile and brittle materials. By collecting the incident, transmitted, and reflected waves during an impact process, the mechanical properties are obtained for the specimen materials loaded at high strain-rates.

Based on the one-dimensional and the stress uniformity assumptions, the strain, strain rate and stress of the specimen can be obtained from equations (1)–(3) [33], respectively,

$$\varepsilon(t) = \frac{2C_0}{L}\int_0^t \varepsilon_R(t)dt \tag{1}$$

$$\dot{\varepsilon}(t) = \frac{2C_0}{L}\varepsilon_R(t) \tag{2}$$

$$\sigma(t) = E\left(\frac{A}{A_S}\right)\varepsilon_T(t), \tag{3}$$

where ε_R and ε_T are the pulse strain amplitudes of the reflected and transmitted waves, respectively; A_s indicates the cross-sectional area of the specimen; L represents the length of the specimen; A is the cross-sectional area of the incident bar; E represents Young's modulus of the specimen; and C_0 is the speed of the elastic wave in the incident bar.

In addition, SHPB is often modified to mimic the mechanical loadings at high strain-rates. Frew *et al* [34] reported a pulse shaping technique on a conventional SHPB apparatus during the high strain-rate compression tests on brittle materials. By shaping the incident pulse, they were able to load the specimen at a constant strain-rate under the dynamically-balanced stress state during the loading process. The accuracy of the compression tests was thus enhanced. In

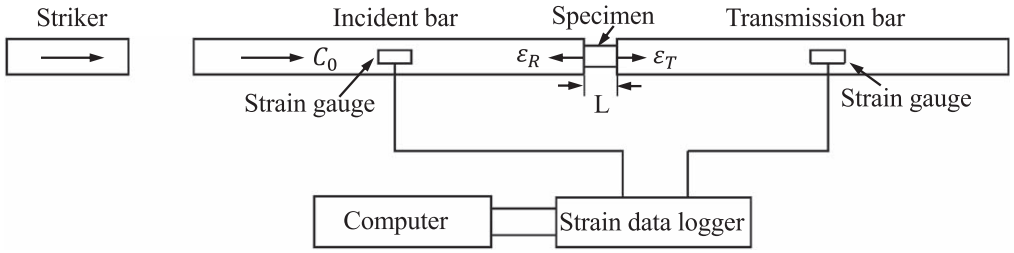

Figure 1. Schematic diagram of SHPB. [33] © Springer-Verlag Wien 2013. With permission of Springer.

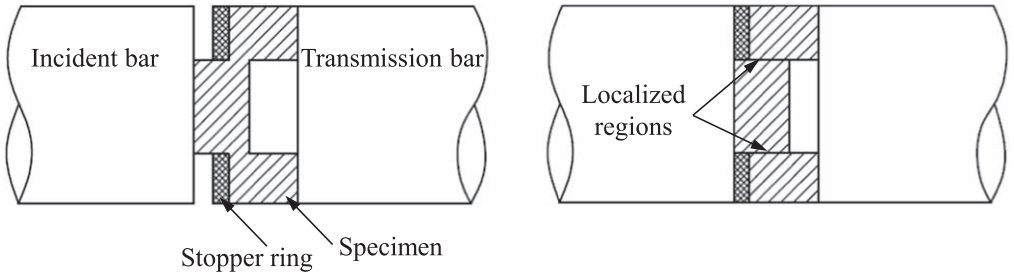

Figure 2. Schematics of the experimental arrangement and the hat-shaped specimen. Reprinted from [37], Copyright 2003, with permission from Elsevier.

Table 2. Strain rates in various high-speed processes.

Processes	Process strain rate	Applications
High-speed machining [11]	Strain rate: 10^3–10^7 s^{-1} Less impact effect	Turning, grinding, milling, sawing, broaching, drilling, etc
Ultrasonically-assisted machining [12, 13]	Strain rate: 10^2–10^6 s^{-1} High impact effect	Base processes: turning, grinding, milling, sawing, broaching, drilling, honing, etc
Shooting [14, 15]	Strain rate: $>10^3$ s^{-1} High impact effect	Meteorite impacting on the space station, bullet shooting, split Hopkinson pressure bar (SHPB), artillery shell shooting, etc
Explosion [16, 17]	Strain rate: $>10^3$ s^{-1} High impact effect	Blasting mining, tunnel blasting, grenade explosion, etc
Structure vibration [18–21]	Strain rate: 10^{-3}–10^2 s^{-1} Less impact effect	Bridge vibration, structure vibration, machine vibration, etc
Tunnel boring [22, 23]	Strain rate: 10^1–10^3 s^{-1} Less impact effect	Highway tunneling, high-speed train tunneling, subway tunneling, underwater tunneling, underground shielding, etc

order to study material responses to higher strain-rates, Liu *et al* [35, 36] built a miniaturized SHPB apparatus with a strain rate of up to 10^4 s^{-1} by strengthening the material and reducing the dimensions of the bar. Although the SHPB technique is widely used on both ductile and brittle materials, it cannot accurately measure the mechanical properties of a material at high strain-rates, e.g. 10^7 s^{-1} which is often associated with the high-speed machining processes.

Meyer *et al* [37] performed a high-speed shear experiment on a hat-shaped specimen using a modified SHPB device, as shown in figure 2. They studied the microstructural evolution of the AISI 304 L stainless steel using electron backscatter diffractometry and transmission electron microscopy. In the experiment, the local strain-rate of the specimen was increased to above 10^4 s^{-1}, which is useful for studying the microstructural evolution in the adiabatic shear band at a high strain-rate. However, the complexity of the stress state within the specimen made it difficult to quantitatively analyze the experimental results.

Sutter *et al* [29] performed a high-speed orthogonal cutting experiment on TC4 using a modified SHPB device, as shown in figure 3. In the experiment, the researchers studied the effects of cutting speed on chip morphology and the mechanisms of chip formation, and found that the chip changed from continuous to discontinuous morphologies with an increase in cutting speed. The experiment allowed them to achieve the orthogonal cutting at a high cutting speed of approximately 75 m s^{-1}. However, it was difficult to control depth of cut in the experiment.

Liu *et al* [38] studied the deformation and fracture behavior of the 7050-T7451 aluminum alloy in an orthogonal cutting experiment at a cutting speed of 120 m s^{-1}, as shown in figure 4. They found that fragmented chips were formed in the mode of brittle fracture, and the material embrittlement

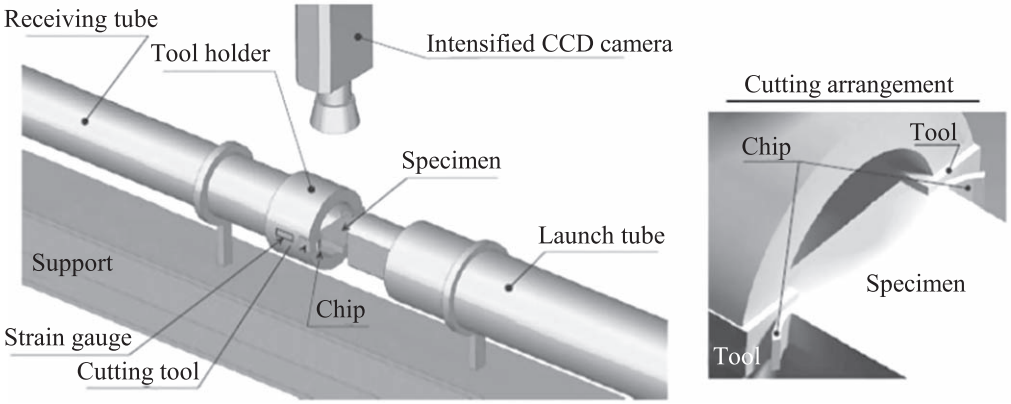

Figure 3. Schematic diagram of the ballistic cutting device. Reprinted from [29], Copyright 2013, with permission from Elsevier.

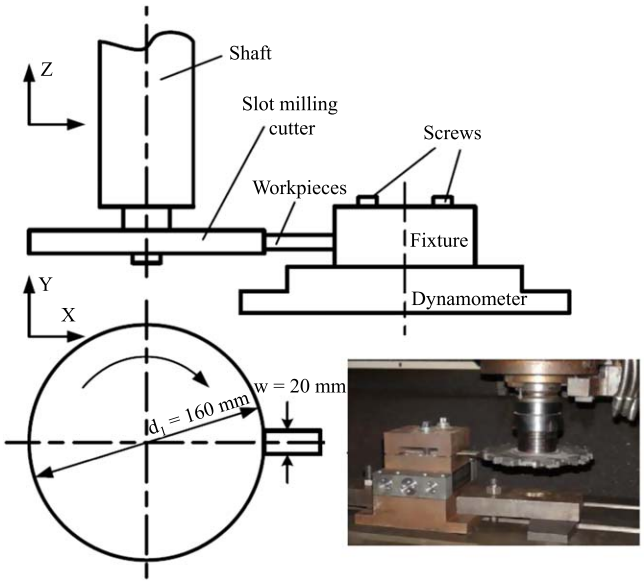

Figure 4. Experimental setup for orthogonal cutting. [39]

leads to the reductions in cutting temperature and cutting force.

Other techniques, including single-point grinding [40], ultrahigh-speed grinding [31], plate impact test [41], SHPB rod test [42], three-axis high-speed impact test [43, 44], expansion ring technique [45], pendulum impact technique [46], projectile penetration [47, 48], etc, are also commonly used to study the material responses to high strain-rates. The above experimental techniques generally have certain limitations, such as insufficient strain-rate or poor cutting accuracy. However, with the rapid development of high-performance machine tools, it becomes possible to conduct ultrahigh-speed machining on difficult-to-machine materials.

2.2. Constitutive material models at high strain-rates

The material responses to dynamic loadings are related to many influencing factors, such as stress/strain fields, strain rate, temperature field, the pre-existing damage, and the surrounding environment. As the number of the factors is overwhelming, it is difficult to experimentally isolate a single factor from the influencing factors. In this regard, constitutive modeling paves an effective way to understanding the material responses to loading at high strain-rates. Generally, the constitutive material models are classified into two types, empirical and physical. Examples are the Johnson and Cook (J–C) empirical model and the physical models based on the dislocation kinetics.

2.2.1. J–C empirical model. The J–C constitutive model is a commonly used empirical model for describing the dynamic mechanical properties of materials. The basic model is shown in equation (4) [49]

$$\sigma = (A + B\varepsilon^n)(1 + C \ln \dot{\varepsilon}^*)(1 - T^{*m}), \tag{4}$$

where σ is the equivalent stress; ε is the equivalent plastic strain; $\dot{\varepsilon}^* = \dot{\varepsilon}/\dot{\varepsilon}_0$ represents the dimensionless strain-rate, $\dot{\varepsilon}_0$ is the reference strain-rate; $T^* = (T - T_r)/(T_m - T_r)$ represents the non-dimensionalized temperature, T_m is the melting temperature of a material, T_r is room temperature; A is the yield strength of a material at the reference strain-rate and temperature; B is the strain hardening coefficient; C represents the strain rate hardening coefficient; n is the strain hardening exponent; and m is the thermal softening coefficient.

The J–C constitutive model considers the effects of strain, strain rate, and temperature on material responses to loading. It has fewer parameters and is widely applied to machining simulations. Being an empirical model, it is different under different material and loading conditions. In order to accommodate material responses to dynamic loading, researchers presented the modified models based on the J–C model, as listed in table 3.

The empirically-based J–C constitutive model is of great significance to solving many practical problems and widely used in the finite element methods at high strain-rates. However, since the model decouples the interplay among strain, strain rate, and heat, which inevitably undermines its prediction accuracy.

For brittle materials, the J–H constitutive model [56, 57] was proposed by Johnson *et al.* The model is shown as equation (5)

$$\sigma^* = \sigma_i^* - D(\sigma_i^* - \sigma_f^*), \tag{5}$$

Table 3. Modified J–C constitutive models.

Reference	Main factor	Constitutive model
Calamaz [50]	Consideration of strain-rate softening	$\sigma = \left[A + B\varepsilon^n\left(\frac{1}{\exp(\varepsilon^a)}\right)\right]\left(1 + C\ln\frac{\dot{\varepsilon}}{\dot{\varepsilon}_0}\right)\left[1 - \left(\frac{T - T_r}{T_m - T_r}\right)^m\right]\left[D + \left(1 - D\tanh\left(\frac{1}{(\varepsilon + S)^c}\right)\right)\right]$
Pan [51]	Effect of recrystallization on yield strength	$\sigma = (A + B\varepsilon^n)\left(1 + C\ln\frac{\dot{\varepsilon}}{\dot{\varepsilon}_0}\right)\left[1 - \left(\frac{T - T_r}{T_m - T_r}\right)^m\right]$ $A = A_{hp} + K_{hp}d^{-1/2}$ $d = d_{drex}X_{drex} + d_0(1 - X_{drex})$
Rule [52]	Correction for strain-rate sensitivity	$\sigma = (A + B\varepsilon^n)\left(1 + C_1\ln\frac{\dot{\varepsilon}}{\dot{\varepsilon}_0} + C_2\left(\frac{\dot{\varepsilon}}{\dot{\varepsilon}_0}\right)^2\right)\left[1 - \left(\frac{T - T_r}{T_m - T_r}\right)^m\right]$
Li [53]	Consideration of hardness effect	$\sigma = [A(HRC) + B\varepsilon^{n(HRC)}]\left(1 + C\ln\frac{\dot{\varepsilon}}{\dot{\varepsilon}_0}\right)\exp\left[-\left(\frac{T^* - m_1}{m_2}\right)^2\right]$
Wang [54]	Temperature effect on strain rate hardening	$C = C_1 - \left[C_2 + C_3\sin\left(\frac{i - 5000}{3000}\pi\right)\right]\sin\left(\frac{T - 500}{150}\pi\right)$
Lin [55]	Coupling effect of temperature and strain rate	$\sigma = (A_1 + B_1\varepsilon + B_2\varepsilon^2)(1 + C_1\ln\dot{\varepsilon}^*)\exp[(\lambda_1 + \lambda_2\ln\dot{\varepsilon}^*)(T - T_r)]$

*For the specific meaning of each parameter, please check the references.

where σ_i^* represents the normalized strength of the intact material; σ_f^* is the normalized fracture stress; and D is the damage factor of the material ($0 \leqslant D \leqslant 1$). The dimensionless expression is represented by

$$\sigma^* = \sigma/\sigma_{\mathrm{HEL}}, \tag{6}$$

where σ_{HEL} is the equivalent stress at Hugoniot elastic limit.

The strength σ_i^* of the intact material can be shown in equation (7)

$$\sigma_i^* = A(P^* + T^*)^N(1 + C\cdot\ln\dot{\varepsilon}^*), \tag{7}$$

where A, C, and N are the material constants to be determined; $\dot{\varepsilon}^* = \dot{\varepsilon}/\dot{\varepsilon}_0$ is the dimensionless strain-rate; $\dot{\varepsilon}$ is strain rate; ε_0 is the reference strain-rate; $P^*$and T^* are the dimensionless pressure and the dimensionless maximum tensile strength, respectively,

$$P^* = \frac{P}{P_{\mathrm{HEL}}} \tag{8}$$

$$T^* = \frac{T}{P_{\mathrm{HEL}}}, \tag{9}$$

where P_{HEL} is the pressure at Hugoniot elastic limit; P is the actual pressure; and T is the maximum tensile strength of a material.

The dimensionless strength of the partially damaged material σ_f^* is

$$\begin{cases} \sigma_f^* = B(P^*)^M(1 + C\cdot\ln\dot{\varepsilon}^*) \\ \sigma_f^* \leqslant \sigma_{f\,\max}^* \end{cases}, \tag{10}$$

where B and M are material constants; and $\sigma_{f\,\max}^*$ is the dimensionless fracture strength of a material. The J–H constitutive model accounts for damage of a brittle material and has widely been used in engineering design of brittle materials, such as concrete and ceramics.

2.2.2. Physically-based models. Dislocation proliferation and slip movement cause plastic deformation in a material. Theoretically, slip could reach the sound speed in a material if no barriers (e.g. grain boundaries and second phase) were present in the material. Thus, the flow stress of the material is usually expressed as equation (11) [58]

$$\sigma_y = \sigma_{pn} + \sigma_{\mathrm{dis}} + \sigma_{\mathrm{HP}} + \sigma_{\mathrm{obs}}, \tag{11}$$

where σ_{pn} represents lattice resistance which is related to temperature and strain rate; σ_{dis} represents interaction forces among dislocations, $\sigma_{\mathrm{dis}} = Gb\sqrt{\rho}$ where G is shear modulus; b is the Burgers vector; ρ is dislocation density; σ_{HP} represents the resistance of grain boundaries to dislocations which can be expressed by the Hall–Petch equation, i.e. $\sigma_{\mathrm{HP}} = k_y d^{-1/2}$, where k_y is a constant; d is the average diameter of material grains; σ_{obs} represents the resistance of the dispersive barriers to dislocations such as segregation and point defects.

The thermal activation theory is commonly used in the study of physically-based models. According to the theory, flow stress σ_y can be decomposed into a short-range component σ_{th} which is thermally related and a long-range component σ_{ath} which is athermal,

$$\sigma_y = \sigma_{\mathrm{th}} + \sigma_{\mathrm{ath}}. \tag{12}$$

Based on the thermal activation theory, the thermal barriers vary with temperature, as shown in figure 5, the stress for dislocations to overcome the barriers decreases as temperature increases. In order to graphically describe the barriers, Follansbee *et al* [59] proposed the following equation to graphically describe the barriers with two

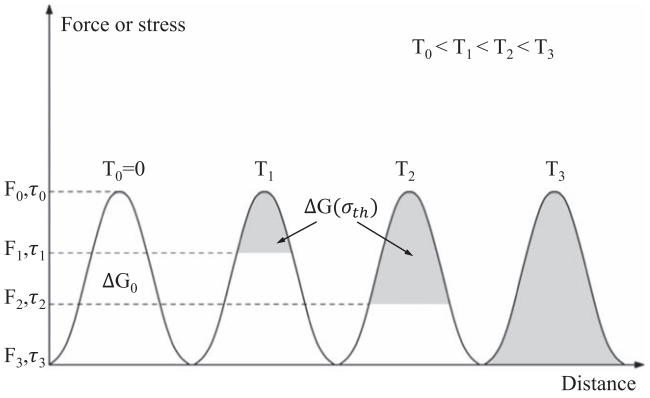

Figure 5. Thermally-activated dislocation to overcome barriers. Reprinted from [60], Copyright 2002, with permission from Elsevier.

parameters, p and q [60]

$$\Delta G = \Delta G_0 \left[1 - \left(\frac{\tau}{\tau_0}\right)^p\right]^q, \tag{13}$$

where ΔG denotes the activation energy of the dislocations to overcome the barriers; ΔG_0 is the energy of the dislocations required to overcome barriers at zero temperature; τ_0 is the flow stress at zero temperature; and τ is the flow stress.

A dislocation overcomes the barrier when its energy exceeds the energy level of the barrier. As the amplitude of the atomic vibration increases with temperature, some dislocations successfully overcome the barriers at a certain frequency v which is given in equation (14)

$$v = v_0 \exp\left(-\frac{\Delta G}{kT}\right), \tag{14}$$

where v_0 is the vibrational frequency of a dislocation; k is Boltzmann's constant; T is temperature; $t_w = v^{-1}$, where t_w is the time a dislocation spends waiting at a barrier for thermal activation. The dislocation moves in-between the barriers at a velocity of v_f that can be shown in equation (15) [61],

$$b\sigma_f = Bv_f, \tag{15}$$

where B is the drag coefficient; σ_f denotes the dislocation slip driving force $\sigma_f = \sigma_y - \sigma_{\text{ath}}$. Assuming that l is the average distance between the successive barriers, slip time t_f of the dislocation in-between the barriers is

$$t_f = \frac{l}{v_f}. \tag{16}$$

The average speed of the dislocation is given as [62]

$$V = \frac{l}{t_w + t_f}. \tag{17}$$

At a low strain-rate, $t_w \gg t_f$, the dislocation drag can be ignored, whereas at a high strain-rate, $t_w \approx t_f$, the dislocation drag is significant and cannot be ignored. Table 4 lists some of the physically-based models for material deformation at high strain-rates.

The physically-based models are helpful in understanding the effects of strain rate on material properties and dislocation density. However, the physically-based models are complicated, which limits their practical applications.

2.3. Material responses to dynamic loading

Figure 6 shows the effect of strain rate on the yield strengths of the materials based on different models. The black data points fitted with the solid lines and the white data points fitted with the broken lines are the calculation results based on the physical and empirical models, respectively. The results from the physical models show that the yield strengths of the materials rapidly increase when strain rate is beyond approximately $10^4\,\text{s}^{-1}$, which is also verified by many researchers in their experimental studies. The results suggest that the dislocation drag be a dominant factor in material deformation at high strain-rates [68–71]. From this respect, the physically-based models can more accurately describe the strain-rate effects on material properties than does the J–C model.

Figure 7 presents the experimental results of shear stress with shear strain rate for single crystalline aluminum. Although the influences of the second phase and grain boundaries are absent, the results show that the dislocation drag is also significant for single crystalline aluminum, indicating that the dislocation drag is related to the dislocation interactions and lattice resistances.

Numerous results show that material strength (yield strength and ultimate tensile strength, etc) increases with strain rate. Zhou *et al* [31] suggested that the yield strength of a material should approach the ultimate tensile strength with an increase in strain rate. When the yield strength of a material is larger than the ultimate tensile strength, the material undergoes brittle fracture without plastic deformation. Material embrittlement thus occurs. Assuming that the difference between the ultimate tensile strength and the yield strength is $\Delta\sigma$

$$\Delta\sigma = \sigma_{\text{UT}} - \sigma_{\text{Y}}, \tag{18}$$

where σ_{UT} is the ultimate tensile strength; σ_{Y} is the yield strength. Figure 8 shows the change in $\Delta\sigma$ with strain rate for different materials. The results in figure 8 are summarized from the research conducted by the different researchers [42, 76–80]. From figure 8, a relationship between $\Delta\sigma$ and strain rate is obtained and shown in equation (19)

$$\Delta\sigma = k_0 - k_s \ln \dot{\varepsilon}, \tag{19}$$

where k_0 is a material constant; k_s represents strain-rate sensitivity on material embrittlement. A material undergoes the ductile-to-brittle transition at $\Delta\sigma = 0$, k_s is different for different materials. According to the values of k_s shown in figure 8, materials can be divided into three types: I, II, and III, among which the type I materials are of the largest k_s and the most susceptible to embrittlement at high strain-rates, whereas the type III materials are the least sensitive to strain rates and the least susceptible to embrittlement at high strain-rates. For example, TC4 and DP1000 are the type I materials with their strain-rate sensitivities of 35.4 and 45.9, respectively. $\Delta\sigma$ of

Table 4. Physically-based models for material deformation at high strain-rates.

References	Constitutive model
Z-A [63]	FCC: $\sigma = \Delta\sigma_G + c_2\varepsilon^{1/2}\exp(-c_3T + c_4T\ln\dot{\varepsilon}) + kl^{-1/2}$ BCC: $\sigma = \Delta\sigma_G + c_1\exp(-c_3T + c_4T\ln\dot{\varepsilon}) + c_5\varepsilon^n + kl^{-1/2}$
MTS [64]	$\sigma = \hat{\sigma}_a + (\hat{\sigma} - \hat{\sigma}_a)\left\{1 - \left[\frac{KT\ln(\dot{\varepsilon}_0/\dot{\varepsilon})}{g_0\mu b^3}\right]^{1/q}\right\}^{1/p}$
S-L [65]	$Y = [Y_T(\dot{\varepsilon}_P, T) + Y_A f(\varepsilon_p)][G(p, T)/G_0]$
Lindgren [66]	$\sigma = \tau_0 Gb\sqrt{\rho_i} f_{DSA}\left(1 - \left(\frac{KT}{\Delta f_0 Gb^3 f_{DSA}}\ln\left(\frac{\dot{\varepsilon}_{ref}\sqrt{\rho_i}}{\dot{\varepsilon}}\right)\right)^{1/q}\right)^{1/p} + m\alpha Gb\sqrt{\rho_i} + G\left(C_e + C_p\frac{T}{300}\right)\dot{\varepsilon}^p$
Zhang [67]	When $\dot{\varepsilon} < \dot{\varepsilon}^{cr}$ $\sigma_f = \sigma_G + \hat{C}\cdot(1 - \exp(-k_0\varepsilon))^{1/2}\left\{1 - \left[-c_2T\ln\left(\frac{\dot{\varepsilon}}{\dot{\varepsilon}_0}\right)\right]^{1/q}\right\}^{1/p}$ When $\dot{\varepsilon} > \dot{\varepsilon}^{cr}$ $\sigma_f = \sigma_G + B[1 - \exp(-k_{a0}\varepsilon)]^{1/2} + \hat{C}\sqrt{\left\{1 + \tanh\left[c_0\log\left(\frac{\dot{\varepsilon}}{\dot{\varepsilon}_{s0}}\right)\right]\right\}\cdot\left(\frac{\dot{\varepsilon}}{\dot{\varepsilon}_{s0}}\right)^{c_1T}\cdot\left\{1 - \exp\left[-k_0\left(\frac{\dot{\varepsilon}}{\dot{\varepsilon}_{s0}}\right)^{-c_1T}\varepsilon\right]\right\}}$

*For the specific meaning of each parameter, please check the references.

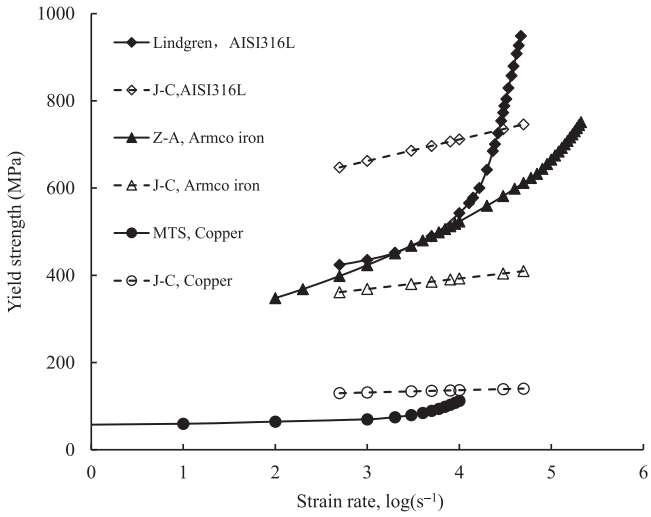

Figure 6. Yield strength versus strain rate results obtained from different models [49, 63, 64, 66, 72–74].

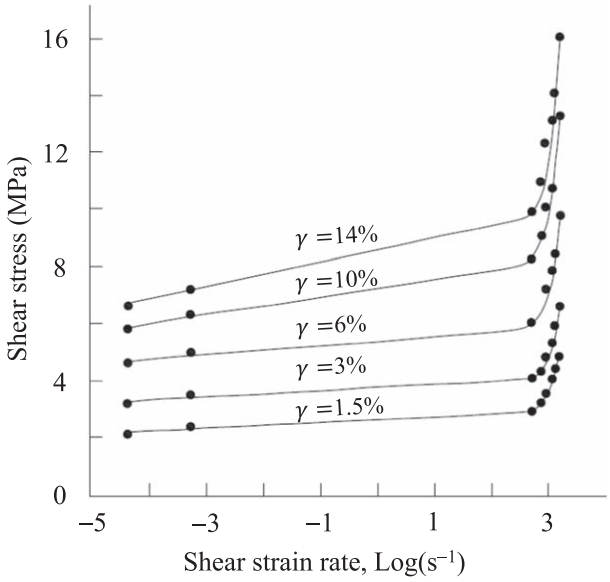

Figure 7. Experimental results of shear stress versus shear strain-rate for single crystalline aluminum. Reprinted from [75], Copyright 1983, with permission from Elsevier.

the type I materials rapidly diminish at an increased strain-rate during a loading process. At $\Delta\sigma = 0$, a material is completely embrittled. Conversely, 7075-T6 and 6061-T6 belong to the type III materials with their respective k_s values of 1.5 and 0.4. Material embrittlement is difficult to occur even if at a very high strain-rate. For the materials with the same k_s, the larger the k_0, the higher the strain rate for material embrittlement.

The effect of strain rate on the property changes of a brittle material is also significant. The commonly used technique is SHPB for studying the property changes of brittle materials at high strain-rates. Harsha *et al* [81] developed a micro-mechanically motivated constitutive model based on crack growth dynamics, and related crack speed to the instantaneous value of stresses at a crack tip. Both the experimental and simulation results are shown in figure 9. It can be seen that similar to the materials depicted in figures 6 and 7, the material strength of a marble also rapidly increased as strain rate was increased to 10^3 s^{-1}, which is attributed to the understanding that the interplay of the nonlinear and

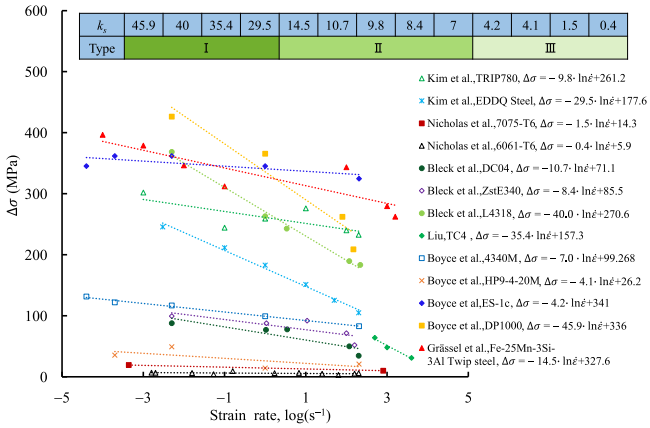

Figure 8. Effects of strain rate on $\Delta\sigma$ [42, 76–80].

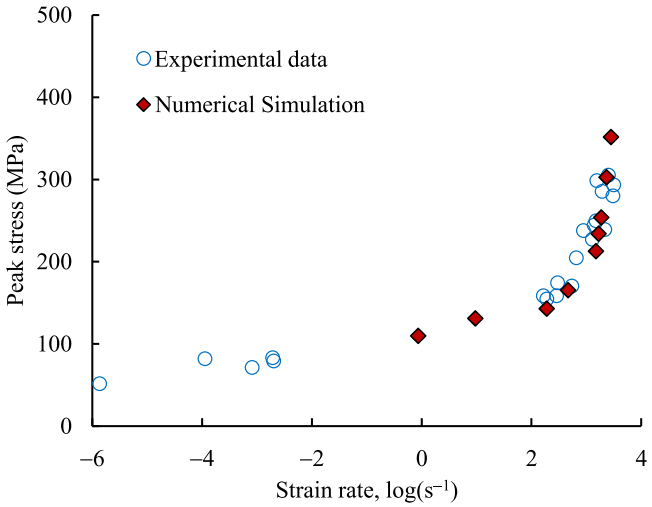

Figure 9. Effects of strain rate on the strength of marble. Reproduced with permission from [81].

inertial effects associated with the propagating crack tip may create a material resistance at the crack tip to interfere with crack propagation [82, 83].

Li *et al* [84] studied the variation of the strength and fragment size of a granite with strain rate under impact loading and found that with an enhanced strain-rate, the strength of the granite went up but the fragment size came down. Figure 10 shows the results of an impact test on the aluminosilicate glass and a similar conclusion was obtained [85]. Grady and Kipp *et al* [86] explained that at a higher strain-rate, more defects might be activated in the material, resulting in material fragmentation with smaller fragments and debris.

For amorphous materials such as metallic glass, strain rate can also significantly affect the material properties [87, 88]. Lu *et al* [89] studied the static and dynamic mechanical properties of Zr-based bulk metallic glass using quasi-static and dynamic SHPB loading devices, respectively. They showed that the material strength increased with strain rate. Yu *et al* [90] performed tensile tests on La-based metallic glass with different strain-rates and temperatures, and found that an increase in strain rate promoted embrittlement of the metallic glass. Liu *et al* [35] used a modified SHPB device to perform dynamic compression experiments on a Zr-based bulk metallic glass and found that the superplasticity of the material disappeared with an increase in strain rate. Therefore, an increase in strain rate can also lead to material embrittlement of an amorphous material.

The above studies show that the material strengths increase with strain rate up to a critical value. In addition, the increase in strain rate leads to material fragmentation, which will be discussed in the next section.

3. Material embrittlement at high strain-rates

3.1. Material embrittlement in machining processes

During a machining process, such as high-speed machining, ultrasonically-assisted machining, and tunnel boring, material embrittlement can be induced. As shown in figure 11, in an orthogonal cutting process, cutting chips change from the continuous to discontinuous types at an increased cutting speed. In high-speed machining, strain rate is up to $10^7\ s^{-1}$ [91–93]. Material removal mechanism in high-speed machining is quite different from that in the conventional machining. Wang *et al* [94] studied the ductile-to-brittle transition in machining and found that as strain rate increased, chip morphology changed from the continuous to discontinuous types. Ma *et al* [95] carried out a high-speed orthogonal cutting experiment of TC4 on a modified SHPB and found that the brittle fracture occurred on the free surface of the chips. They also found that brittle fracture increased while ductile fracture decreased with an increase in cutting speed.

Ultrasonically-assisted machining is a viable method for machining of many different materials, especially hard and brittle materials. In an ultrasonically-assisted machining process, a cutting tool is superimposed with high-frequency vibration to obtain a much higher instantaneous cutting speed and acceleration than those in a regular cutting process. The higher speed and acceleration lead to a high strain-rate which may evoke material embrittlement in the machining process. Zhao *et al* [97] studied the ultrasonically-assisted machining of rocks, and found that an increase in the impact frequency could significantly reduce strength and increase fragmentation of the material; Lv *et al* [98] studied the ultrasonically-assisted machining of the BK7 glass, and demonstrated that the ultrasonic vibrations caused material fragmentation and a reduced cutting force. In their experimental study on the K9 glass, Wang *et al* [99] found that the ultrasonically-assisted machining could reduce the depth of subsurface damage by 30%–40% compared to that in the conventional machining.

A material is embrittled and fragmented in an ultrasonically-assisted machining process because of the high strain-rates involved in the process. As shown in figure 12, the influence of strain rate on material embrittlement and subsurface damage can be explained as follows.

(1) The material resistance ahead of a crack tip increases with strain rate, impeding crack propagation.

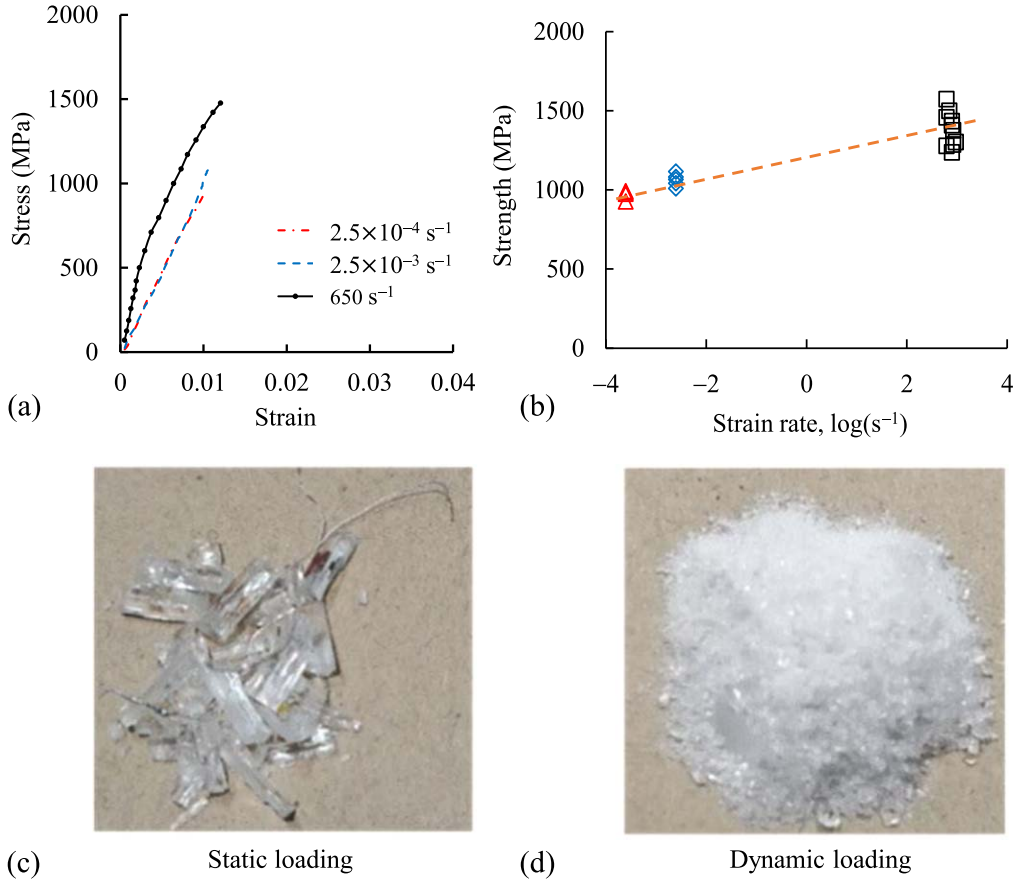

Figure 10. The results of the dynamic compression experiments of an un-strengthened aluminosilicate (ALS) glass. (a) The representative curves obtained in the static and dynamic tests; (b) the maximum compression strength against strain rate; (c) the collected fragment and debris from static and (d) dynamic loading tests. Reprinted from [85], Copyright 2018, with permission from Elsevier.

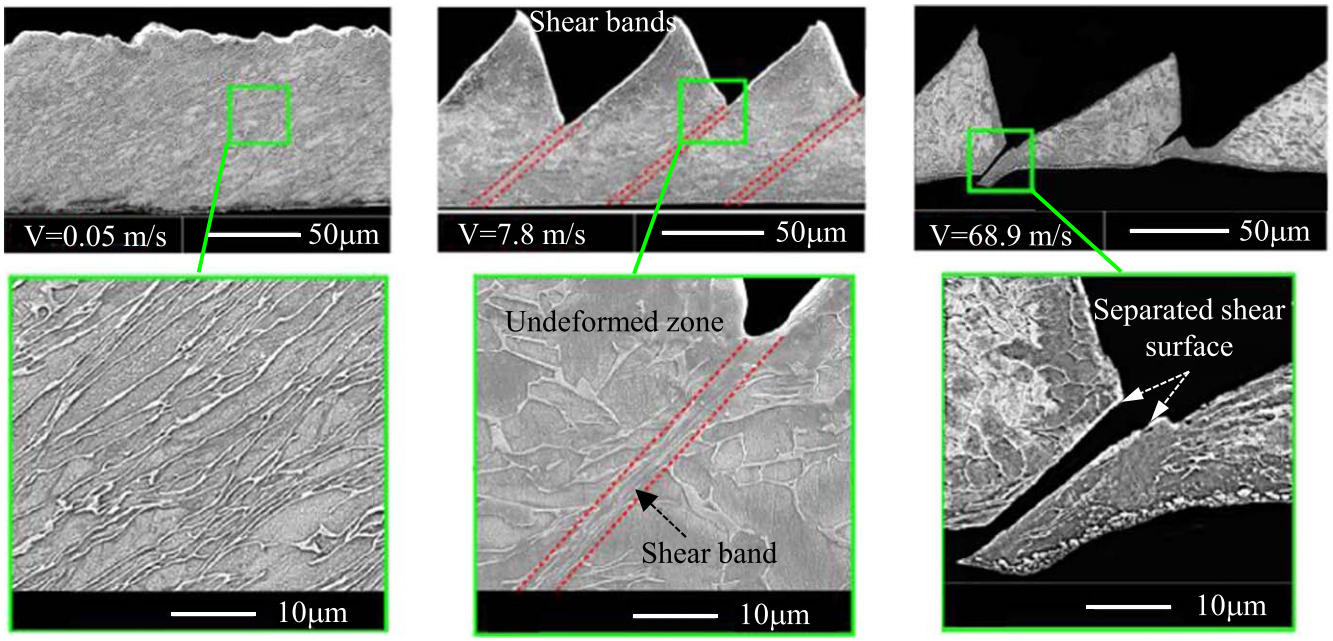

Figure 11. Chip morphologies of TC4 at different cutting speeds. [96] © Springer-Verlag London 2016. With permission of Springer.

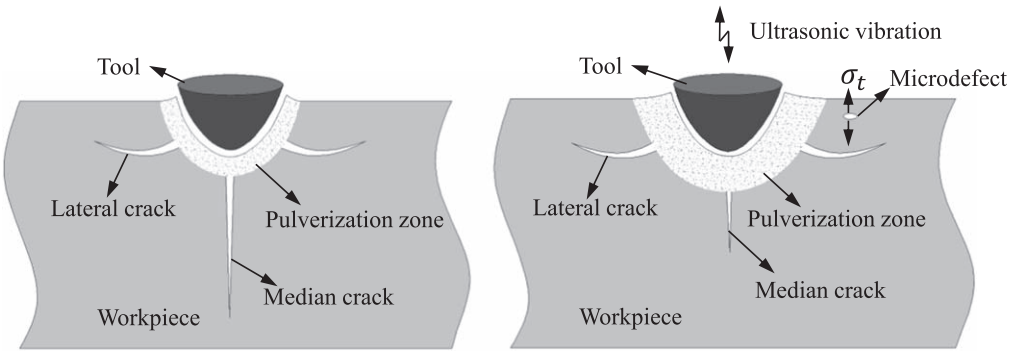

(a) Conventional machining (b) Ultrasonically-assisted machining

Figure 12. Material damage induced in conventional machining and ultrasonically-assisted machining.

(2) The directions of cutting and median crack propagation are different in a machining process. At a higher cutting speed, a median crack, if nucleated, has less time to propagate before the cutting tool passes by, resulting in smaller depth of subsurface damage.
(3) The internal defects of a material are activated under impact loading, which triggers nucleation, propagation, and interdigitation of microcracks, and more fragmentation and pulverization in the surface layer of the material.

A tunnel boring machine (TBM) is normally applied to cutting hard and brittle rocks encountered in boring tunnels for subways and trains. Material embrittlement, fragmentation, and pulverization also exist in the boring processes of a tunnel. The brittleness of a rock is enhanced in a boring process due to the strain-rate effect, and can in turn significantly influence the machinability of the rock. Kahraman *et al* [100] studied the methods of measuring material brittleness and the correlations between brittleness and machinability of rocks, and suggested that there should be an exponential correlation between the boring performance of a TBM and the brittleness of a rock; Gong *et al* [101] studied the influence of rock brittleness on TBM penetration rate, and found that the crushed zone and radial cracks increased with rock brittleness and the failure element induced by the cutter almost linearly increased with rock brittleness. In order to improve machining efficiency and reduce tool wear, Wu *et al* [102] presented a rock fragmentation method of shock disturbance, and established a crack model for the damaged rock around an induced hole, and observed that the penetration rate increased with crack density, whereas the cutting force decreased with the increase in the disturbance frequency. Increasing rock brittleness through an enhanced strain-rate is obviously beneficial to improving machinability and efficiency in the tunnel boring process.

In a machining process, high strain-rate evokes not only embrittlement but also fragmentation of a material. The fragment size S of brittle materials at high strain-rates was evaluated by Zhang *et al* [103], as shown in equation (20). It can be shown that the average fragment size decreases with an increase in strain rate

$$S = \frac{6K_{IC}^2}{D_f E^2 \dot{\varepsilon}^2 t_f^2}, \tag{20}$$

where K_{IC} is the fracture toughness of a material; D_f denotes the damage scalar corresponding to the initiation of fragmentation; E is Young's modulus; and t_f is the total time to reach the fracture stress. In addition, Grady and Kipp *et al* [104] conducted an expansion ring impact test for ductile materials, and calculated fragment size S based on the fracture energy theory, as shown in equation (21)

$$S = \left(\frac{12\gamma_s}{\rho_0 \dot{\varepsilon}^2}\right)^{1/3}, \tag{21}$$

where γ_s is surface energy; and ρ_0 is material density.

3.2. Effects of stress wave on material fragmentation

Stress wave is an important factor affecting material fragmentation under high strain-rate. Material fragmentation is related to the process of stress wave propagation, reflection, and interaction. Zhang *et al* [105] believed that stress wave response caused by impact loading was the main cause of material removal and crack formation in hard and brittle materials. Based on the propagation state of stress waves in a solid, there are different modes for stress wave propagation, such as elastic, plastic, and viscoelastic waves. The propagation velocities of the elastic and plastic waves are shown in equations (22) and (23), respectively [106]

$$v_e = \left(\frac{E}{\rho_0}\right)^{1/2} \tag{22}$$

$$v_p = \left(\frac{1}{\rho_0}\frac{d\sigma}{d\varepsilon}\right)^{1/2}, \tag{23}$$

where E represents Young's modulus of the material; $d\sigma/d\varepsilon$ is the slope of the tangent line corresponding to the point of stress σ on the stress-strain curve; ρ_0 is the density of the material. It can be understood that propagation of stress waves is related to the mechanical properties of a material under impact loading.

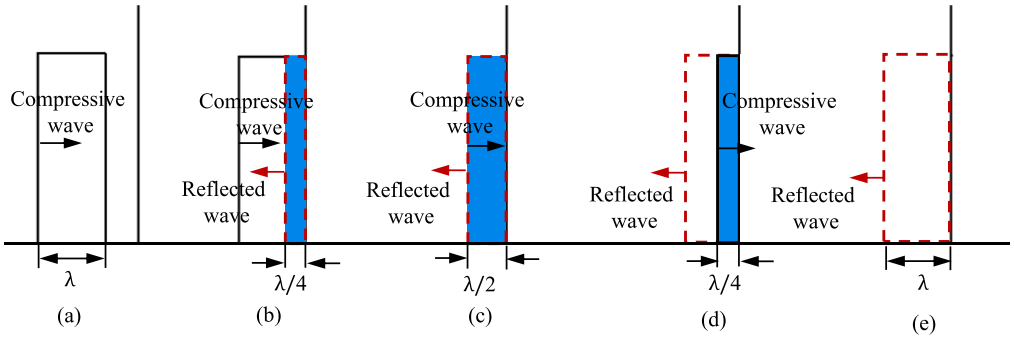

Figure 13. Compressive stress wave propagation and reflection at the free surface. Reprinted from [107], Copyright 2011, with permission from Elsevier.

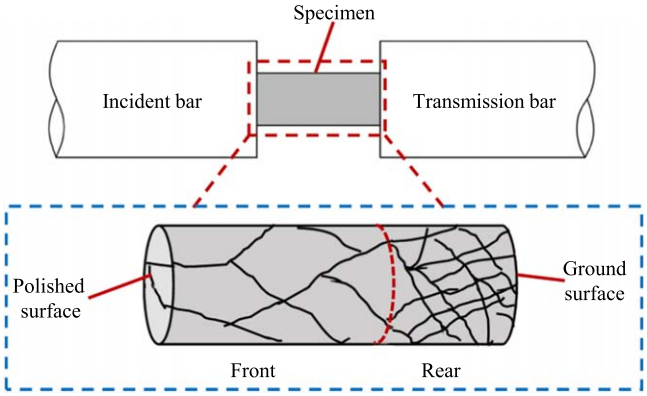

Figure 14. Schematic diagram of fracture characteristics at high strain-rates for granite. Reproduced with permission from [108].

Material damage can be caused by the stress waves that are generated during impact loading, and propagate to and are reflected from the free surface of a material. Figure 13 shows the pressure distribution at different times when the compressive wave with a wavelength λ is reflected at the free surface of a rod end [107]. In figure 13(a), the compressive wave is close to the free surface; (b) the incident compressive wave and the reflected tensile wave are superposed to form a composite wave, and tensile stress appears in the overlap region (in blue); (c) the composite wave is in tensile, which represents a critical state. Before the state, the rod is still subjected to partial compressive stress. After the state, the rod is completely subjected to tensile stress; (d) the overlap region and the tensile stress are gradually reduced; (e) the incident compressive wave fades and the stress wave reflection ends. As shown in figure 14, Jiang *et al* [108] carried out an impact compression experiment on a granite by SHPB and studied the fracture characteristics of the granite under an impact load. The reflection of an incident compression wave on the ground surface can cause a tensile wave and eventually induce tensile stress near the ground surface, resulting in crack nucleation and propagation, and thus material fragmentation in the rear portion of the specimen.

Figure 15 shows the stress wave propagation process when top of the cylinder receives an impact load. Cracks are formed during the impact loading process, as shown in figure 15(c). The OA crack is caused by the encounter of the reflected tensile waves in the middle of the cylinder; the BC crack is due to the reflected tensile wave from the cylindrical surface; the EF crack is induced by the reflection tensile wave from the bottom surface; the tensile waves are reflected from the bottom and cylindrical surfaces meet at the bottom corner to form crack LM. The crack system in figure 15 can be evidenced by the material fragmentation of a granite subjected to impact loading, as shown in figure 16. The granite has a crack system of radial cracks that extend outward from the impact center and circumferential cracks that are around the impact center. If the impact load is large enough, the cracks are interdigitated and finally form a massive crumb.

In a ductile material, stress waves can also cause material embrittlement. Liu *et al* [110] carried out a projectile impact test on a titanium alloy target. Figures 17(a) and (c) display a cross-sectional view and stress field of the target during the projectile impact process, respectively. No plastic deformation was observed in zones I and III, which depicts that brittle fracture was the dominant mode of deformation during the impact process. Meanwhile, the simulation results demonstrated large tensile stresses in zones I and III, which verifies the results obtained in the impact test.

Zheng *et al* [111] also conducted an armor-piercing projectile test on TC4 at an impact velocity of 820 m s^{-1}, and studied the failure mechanisms of a TC4 material, and found a large number of microcracks left in the TC4 material by the projectile piercing, as shown in figure 18. They reported that the microcracks propagated and coalesced into macroscopic cracks. The TC4 material was thus embrittled in the surrounding area of the piercing hole. It can be observed from figure 18 that the material surrounding the hole was pushed and squeezed by the projectile and was left with a large number of cracks along the fibrous/lamellar layers in the deformed material. The fibrous/lamellar layers might be due to a combination of the tensile stress caused by the head and the compressive stress of the body of the projectile during the penetration process.

3.3. Critical conditions for material embrittlement at high strain-rates

Rice and Thomson [112] established a criterion for brittle fracture of crystalline materials in terms of the spontaneous emission of dislocations from an atomically sharp cleavage

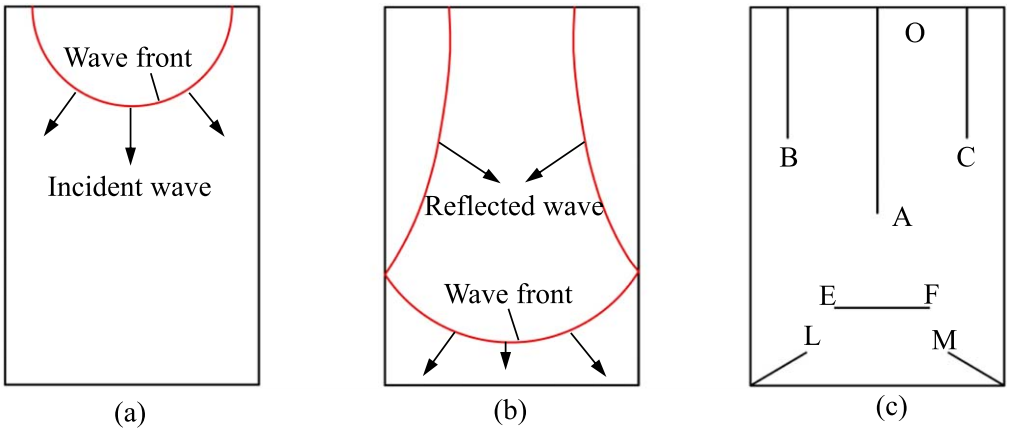

Figure 15. Stress wave propagation when the top of a cylinder is subjected to impact loading. Reprinted from [107], Copyright 2011, with permission from Elsevier.

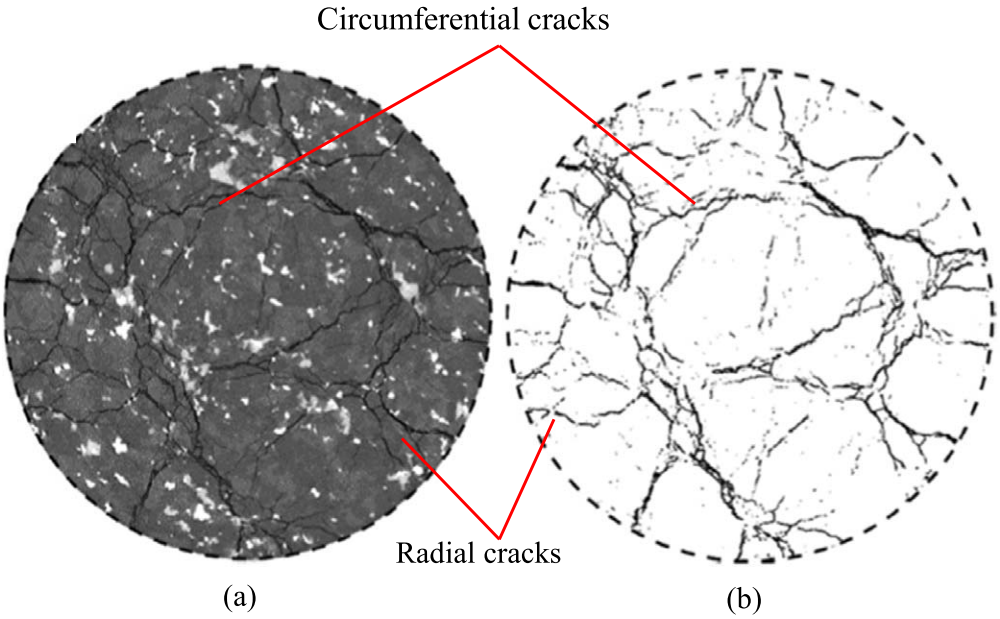

Figure 16. Computed tomography (CT) images: (a) grey image; (b) crack pattern image. Reprinted from [109], with the permission of AIP Publishing.

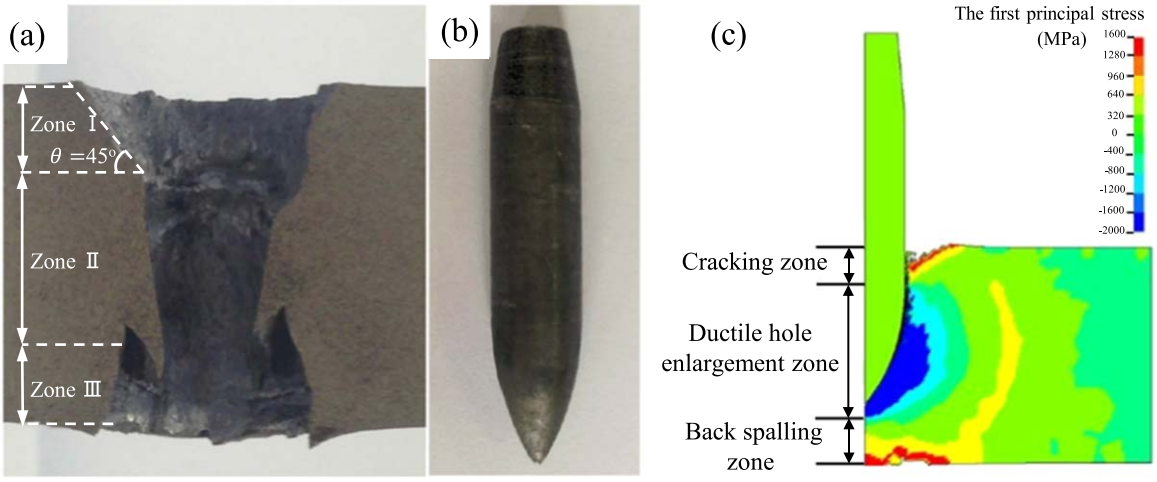

Figure 17. Macroscopic failure characteristics of TC4 titanium alloy target. (a) Failure characteristics; (b) the projectile after impact; (c) first principal stress distribution inside the target during the projectile impact. Reprinted from [110], Copyright 2015, with permission from Elsevier.

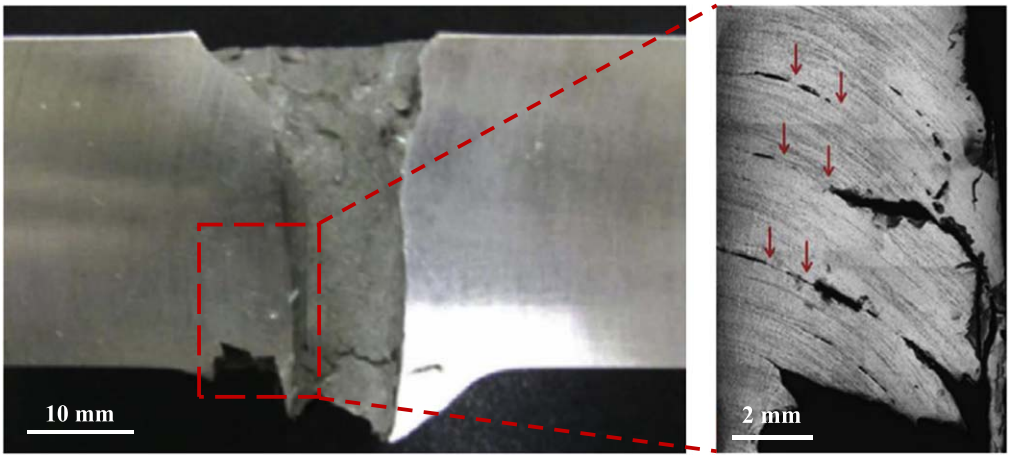

Figure 18. Optical micrographs of the sectioned TC4 target left with numerous cracks by the projectile. Reprinted from [111], Copyright 2015, with permission from Elsevier.

crack and suggested that the materials should be embrittled if the condition in equation (24) were satisfied

$$Gb/\gamma_s \geqslant 7.5 - 10, \tag{24}$$

where G is shear modulus; and b is the Burgers vector. However, the surface energy of a material is difficult to correctly measure, which limits the practical applications of equation (24).

In a study on ductile-to-brittle transition of a material in a high-speed machining process, Zhou *et al* [31] indicated that the material should have been embrittled when cutting speed v_c exceeded plastic wave propagation speed v_p, as presented in equation (25),

$$v_c > v_p = \left(\frac{1}{\rho_0}\frac{d\sigma}{d\varepsilon}\right)^{1/2}. \tag{25}$$

Wang *et al* [113] also studied material embrittlement in a high-speed orthogonal cutting process and found that material embrittlement occurred at $v_c > v_p$. However, problems occur if the propagation speed of a plastic wave is taken as the critical cutting speed for the ductile-to-brittle transition of a material.

(1) Generally, strain rate is proportional to cutting speed. It can alter the properties of a material, and further change the plastic wave propagation speed of the material.
(2) The microdefects and stress states of the material have important influences on damage formation and fracture of the material. It is hard to accurately describe the ductile-to-brittle transition of the material solely with the critical cutting speed.

Lawn *et al* [114] were the first to define brittleness using the ratio of hardness H to toughness K_f for hard and brittle materials. Zhang *et al* [30] studied the relationship between brittleness and subsurface damage depth for hard and brittle materials and were the first to report that subsurface damage depth is inversely proportional to material brittleness.

For ductile materials, Campbell *et al* [115] investigated the influences of strain rate $\dot{\varepsilon}$, temperature T, and grain size D on tensile fracture strain of the En2A steel, and found that tensile fracture strain decreased with an increase in strain rate, as shown in figure 19. Similarly, in their experimental study on

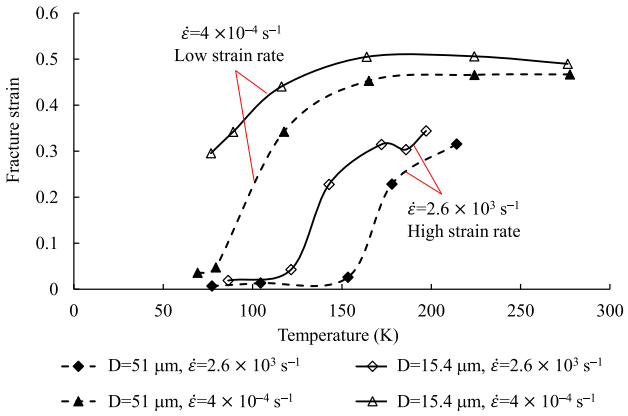

Figure 19. Effects of strain rate, temperature, and grain size on tensile fracture strain of the En2A steel. [115] 2018 Reprinted by permission of the publisher (Taylor & Francis Ltd, http://www.tandfonline.com).

the ductile-to-brittle transition of an Ni metal, Mahalingam *et al* [116] found that the toughness of the metal decreased with an increase in strain rate. Abushawashi *et al* [117] also studied the influence of strain rate on the fracture strain of a material during a cutting process. The fracture strain was calculated based on the J–C damage model, as shown in equation (26)

$$\varepsilon_f = C_1 e^{C_2\eta_f}\left[1 + C\ln\left(\frac{\dot{\varepsilon}}{\dot{\varepsilon}_0}\right)\right]^{\frac{-2}{n+2}}, \tag{26}$$

where C_1 and C_2 are the material fracture constants to be determined experimentally; η_f represents stress state.

Toughness of a material is a function of strain, strain rate, and temperature, and can be obtained by a material constitutive model $\sigma = f(\varepsilon, \dot{\varepsilon}, T)$ and fracture strain ε_f, as shown in equation (27),

$$K_f = \int_0^{\varepsilon_f} f(\varepsilon, \dot{\varepsilon}, T)d\varepsilon. \tag{27}$$

According to section 2.3, an increase in strain rate leads to an increase in yield strength but a decrease in toughness of a material to evoke material embrittlement, as shown in

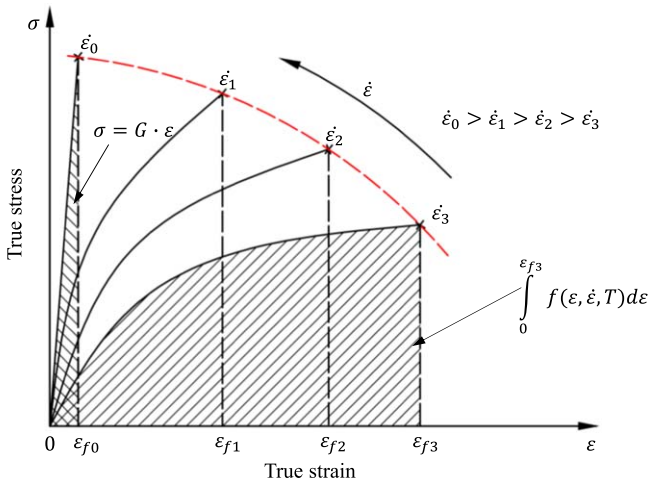

Figure 20. Schematic diagram describing the effect of strain rate on strength and toughness of a material.

figure 20. Therefore, material brittleness B can also be expressed by a ratio of yield strength σ_Y to toughness K_f, as presented in equation (28)

$$B = \frac{\sigma_Y}{K_f}, \tag{28}$$

where $\sigma_Y = f(\varepsilon, \dot{\varepsilon}, T)_{0.2\%}$. At the 0.2% strain, both strain and temperature rise may be ignored, the yield strength equation is thus reduced to $\sigma_Y = f(\dot{\varepsilon})_{0.2\%}$. From equations (27) and (28), material brittleness can be shown as equation (29),

$$B = \frac{f(\dot{\varepsilon})_{0.2\%}}{\int_0^{\varepsilon_f} f(\varepsilon, \dot{\varepsilon}, T)d\varepsilon}. \tag{29}$$

It is worth noting that material strength does not always rapidly increase with strain rate, which is schematically shown in figure 20. The red broken line represents the trend of material strength change with strain rate. A material may encounter a strength limit if it is loaded at an extremely high strain-rate.

3.4. Crack nucleation and propagation

Brittle fracture of a material originates from the nucleation and propagation of cracks. The atomic bond fracture is an important feature in the process of crack nucleation and propagation and is the dominant factor for brittle fracture of a material. The theoretical fracture strength σ_m of a material can be calculated in equation (30)

$$\sigma_m = \left(\frac{E\gamma_s}{a_0}\right)^{1/2}, \tag{30}$$

where E represents Young's modulus of the material; γ_s indicates the surface energy; and a_0 is the lattice constant.

In order to explain the reason why theoretical fracture strength is much larger than the actual fracture strength of a material, Griffith *et al* [118] hypothesized that internal defects reduced the fracture strength of a material, and proposed the Griffith fracture criterion for crack propagation, as shown in

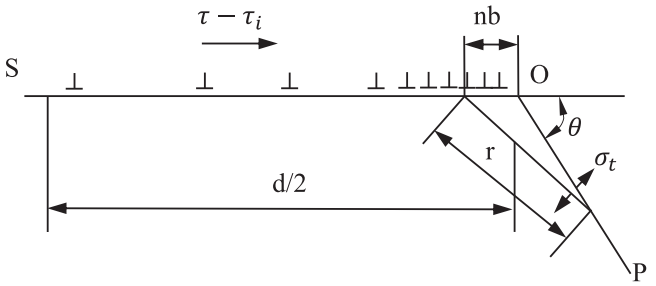

Figure 21. Dislocation pile-up leading to microcrack nucleation.

equation (31),

$$\sigma_c = \left(\frac{2E\gamma_s}{\pi c}\right)^{1/2}. \tag{31}$$

However, the Griffith fracture criterion is only applicable to brittle materials. Orowan *et al* [119] corrected the Griffith fracture criterion and proposed that the energy consumed in front of a crack tip included not only fracture surface energy γ_s but also plastic deformation energy γ_p. The critical condition for crack propagation is presented in equation (32),

$$\sigma_c = \left(\frac{E(2\gamma_s + \gamma_p)}{\pi c}\right)^{1/2}. \tag{32}$$

In order to explain crack propagation mechanisms in ductile materials, Stroh *et al* [120] claimed that dislocation pile-up was the main reason for crack nucleation (figure 21). They believed that when maximum tensile stress σ_{fmax} at the pile-up position reached theoretical fracture strength σ_m of a material, cracks should be nucleated. The critical condition for crack propagation is given in equation (33)

$$\tau_c = \tau_i + \left(\frac{2Er\gamma_s}{da_0}\right)^{1/2}, \tag{33}$$

where $d/2$ represents the distance from the dislocation source to the pile-up position; r is the distance between the pile-up position and crack tip; $\tau - \tau_i$ denotes the effective shear stress on the slip plane.

Based on the dislocation reaction, Cottrell *et al* [121] derived the critical condition for crack propagation from the energy point of view and suggested a critical stress,

$$\sigma_c = \frac{2G\gamma_s}{k_y d^{1/2}}. \tag{34}$$

Considering the Hall–Petch relationship and the influence of the stress state, the critical condition for crack propagation is

$$(\sigma_i d^{\frac{1}{2}} + k_y)k_y > 2G\gamma_s q, \tag{35}$$

where q is a coefficient related to the stress state.

Moreover, metallic glasses do not typically have dislocations and grain boundaries since their atomic structures are long-range disordered. As such, their deformation and fracture behaviors are different from metallic alloys, but significantly depend on strain rate and temperature [122]. High strain-rate and/or low temperature can lead to inhomogeneous deformations of metallic glasses. In this case,

strain is concentrated in the spatial layers (shear bands) as thin as 10–100 nm [123–125]. The formation and propagation of shear bands are the main cause of deformation and crack formation in a metallic glass [88, 126].

4. Discussion

Material embrittlement can occur at a high strain-rate. Generally, a high strain-rate may result in dislocation pile-ups, which may block a dislocation source from further emitting dislocations. In a material deformation process, the material may experience atomic bond rupture to nucleate and propagate a crack. Microscopically, a dislocation overcomes the barriers in a loading process at a low strain-rate. Plastic deformation occurs in the material if given a sufficient time. Conversely, if the dislocation does not have enough time to overcome the barriers in the loading process due to a high strain-rate, dislocations pile-up, which triggers crack nucleation. Conclusively, in a high-speed loading process of a ductile material, if strain rate is so high that no plastic deformation should occur before the material is fractured, the material would be subjected to the complete embrittlement. In this case, the ductile material should exhibit a fracture behavior as if it were a typical brittle material. For a brittle material subjected to loading at a high strain-rate, the embrittlement mechanism is also related to dislocations. An increase in strain rate can lead to material embrittlement and fragmentation. In their grinding research of ceramic materials, Zhang *et al* [127] confirmed that grinding damage to the ceramic materials decreased with an increase in material brittleness.

The nucleation and propagation of a crack are closely related to dislocations. During a crack propagation process, the crack tip emits dislocations which may be impeded by the microstructural barriers, such as grain boundaries, resulting in dislocation pile-ups and microcrack nucleations. On the other hand, as a crack tip is always accompanied with dislocations, dislocation density becomes a governing factor for crack propagation. Generally, the higher the dislocation density, the easier the crack propagation. The reason is that new dislocations may be obstructed by the existing dislocations at the crack tip, forming dislocation pile-up, stress concentration, and finally crack propagation. This has also been confirmed in a study conducted by Jones *et al* [128] in which the authors claimed that in a TC4 sheet, strain hardening could slightly accelerate fatigue crack growth for the case when strain hardening was induced prior to crack initiation.

Stress wave propagation is another mechanism that directly contributes to material fragmentation at a high strain-rate. A stress wave originates and propagates from an impact loading source, and may get reflected on a free surface to become a reflection wave. As shown in figure 13, the interactions between the incident and reflected waves can induce tensile stresses, and further crack nucleation and propagation. For example, if a machining process is accompanied with impact loading, stress wave can be initiated in the machining zone and reflected from the free surface of the workpiece. For a significantly large impact load, the tensile stress caused by the incident and reflected waves can result in crack nucleation and material fragmentation.

Macroscopically, an increase in strain rate during a loading process leads to an increase in strength and hardness but a decrease in toughness of a material. The material is thus embrittled. As to the TC4 material, it is a typical two-phase alloy (α and β phases) in which the α phase has the close-packed hexagonal structure with few slip systems. At an increased strain-rate, TC4 is easy to have dislocation pile-ups, crack nucleation and propagation, and material embrittlement. Conversely, aluminum is a face-centered cubic metal with more slip systems. This material is typically easy to deform during a loading process. Therefore, it is relatively difficult to cause dislocation pile-ups and material embrittlement in aluminum.

If a material is going through an embrittlement process due to fast loading at a high strain-rate, e.g. high-speed machining, the mobile dislocations corresponding to that strain rate do not have enough time to respond to the fast loading but turn into temporarily immobile dislocations under the specified loading conditions. The material influenced by loading exhibits pseudo embrittlement and is not actually embrittled upon unloading. The pseudo embrittlement may help suppress plastic deformation and machining damage in a machined workpiece, which can greatly preserve surface integrity for machining.

Strain-rate sensitivity k_s proposed in this study provides a guide for the determination of material embrittlement in terms of strain rate. For example, TC4 has its strain-rate sensitivity of 35.4 which is the 3rd highest among the metallic materials listed in figure 8. Since TC4 is highly strain-rate sensitive, it should be a good candidate material for high-speed machining. High quality and high efficiency machining is thus anticipated.

A material with low strain-rate sensitivity k_s may find applications in energy absorption. An example is an armor made of both aluminum alloy and ceramics that can absorb the energy of a projectile [129–131]. Because the aluminum alloys possess the lowest strain-rate sensitivity among all the materials shown in figure 8, they are not readily embrittled when subjected to loading at a high strain-rate. The armor has a combination of energy absorption through the outstanding plastic deformability of the aluminum alloy and the anti-penetrability of ceramics for an enhanced protectionability from the strike of a high-speed projectile. Temperature rise is another important factor affecting material embrittlement, especially in a machining process. Plastic deformation directly contributes to temperature rise, which is conducive to dislocation movement but inconducive to material embrittlement. In order to study material embrittlement due to the strain-rate effect, it is necessary to minimize the temperature effect. Salomon [132] was the first to propose that in a machining process, machining temperature was expected to have an increase and then a sharp decrease as cutting speed was increased. Unfortunately, the Salomon prediction never becomes a reality although some researchers tried to use different techniques to verify his prediction. The high-speed machining was one of the techniques used by the researchers.

Therefore, more studies are necessary to the investigation of the strain-rate effect on material embrittlement in high-speed machining.

The strain-rate effect is considered as an important influencing factor in the physical and empirical constitutive modeling of a material. Compared with the J–C model, a physical model is more accurate to predict property change of a material subjected to loading at a high strain-rate. However, the physically-based models are generally sophisticated, which limits their practical applications. In this regard, it is necessary to modify the existing constitutive models or to establish a new constitutive model.

5. Conclusions

This study discusses material embrittlement, and the critical conditions for ductile to brittle transition of ductile materials based on the strain-rate effect, and arrives at the following conclusions:

(1) Material embrittlement and fragmentation occur when loading at a high strain-rate.
(2) Strain-rate sensitivity k_s is an inherent property of a material that measures how sensitive the material is to strain-rate evoked embrittlement.
(3) Material embrittlement and fragmentation do not readily occur on a material that has low strain-rate sensitivity, and vice versa.
(4) Strain-rate sensitivity is an important indicator in selecting a material for a specific application, e.g. armor protection and high-speed machining.
(5) Material embrittlement and fragmentation can be caused by stress wave propagation and reflection in a loading process.

Strain-rate evoked material embrittlement can have many industrial applications. Machining, TBM, and armor protection are a few examples that are discussed in this study. More applications are anticipated if the underlying mechanisms are made clear. In machining of difficult-to-machine materials, for example, strain-rate evoked embrittlement may be applicable to many difficult-to-machine materials, such as titanium alloys, aerospace alloys, high temperature alloys, semiconductors, and ceramics. Machining quality and efficiency are expected to have a great improvement.

Although strain-rate evoked material embrittlement has been explored, the fundamental issues are yet to be investigated. Dislocation kinetics, crack nucleation and propagation at high strain-rates are still unclear. Further studies are necessary.

Acknowledgments

The authors would like to acknowledge the supports by the National Natural Science Foundation of China (Grant No. 51575084) and the Peacock Program of Shenzhen (Grant No. KQJSCX20180322152221965).

References

[1] Cottrell A H 1953 *Dislocations and Plastic Flow in Crystals* (Oxford: Clarendon Press)
[2] Koyama M, Shimomura Y, Chiba A, Akiyama E and Tsuzaki K 2017 Room-temperature blue brittleness of Fe-Mn-C austenitic steels *Scr. Mater.* **141** 20–3
[3] Stepanov N, Tikhonovsky M, Yurchenko N, Zyabkin D, Klimova M, Zherebtsov S, Efimov A and Salishchev G 2015 Effect of cryo-deformation on structure and properties of CoCrFeNiMn high-entropy alloy *Intermetallics* **59** 8–17
[4] Darnbrough J, Roebuck B and Flewitt P 2015 The influence of temperature and grain boundary volume on the resistivity of nanocrystalline nickel *J. Appl. Phys.* **118** 184302
[5] Xing X, Yu M, Chen W and Zhang H 2017 Atomistic simulation of hydrogen-assisted ductile-to-brittle transition in α-iron *Comput. Mater. Sci.* **127** 211–21
[6] Toyama T, Nagai Y, Tang Z, Hasegawa M, Almazouzi A, van Walle E and Gerard R 2007 Nanostructural evolution in surveillance test specimens of a commercial nuclear reactor pressure vessel studied by three-dimensional atom probe and positron annihilation *Acta Mater.* **55** 6852–60
[7] Pons D and Bourgoin J 1985 Irradiation-induced defects in GaAs *J. Phys. C: Solid State Phys.* **18** 3839
[8] Kameda J and Bevolo A 1989 Neutron irradiation-induced intergranular solute segregation in iron base alloys *Acta Metall.* **37** 3283–96
[9] Chilton A and Wronski A 1969 The effects of strain rate and pressurization on the ductile-brittle transition temperature of polycrystalline sintered tungsten *J. Less-Common Met.* **17** 447–50
[10] Wang B 2016 Influence mechanism of material deformation and fracture behavior on chip formation during high-speed machining *Doctoral Dissertation* Shandong University
[11] Wang B, Liu Z, Su G, Song Q and Ai X 2015 Investigations of critical cutting speed and ductile-to-brittle transition mechanism for workpiece material in ultra-high speed machining *Int. J. Mech. Sci.* **104** 44–59
[12] Hocheng H and Tai N H 2000 Assessment of ultrasonic drilling of C/SiC composite material *Composites* A **31** 133–42
[13] Tawakoli T and Azarhoushang B 2008 Influence of ultrasonic vibrations on dry grinding of soft steel *Int. J. Mach. Tools Manuf.* **48** 1585–91
[14] Iqbal M A, Gupta G, Dikawar A and Gupta N K 2010 Effect of projectile nose shape on the ballistic resistance of ductile targets *Eur. J. Mech.* A **29** 683–94
[15] Klavzar A, Pursche F, Herzig N and Wolf T 2017 Ballistic limit thickness and failure of steel targets with different strengths under EFP impact *Proc. Eng.* **197** 270–7
[16] Hiroe T, Fujiwara K, Hata H and Takahashi H 2008 Deformation and fragmentation behaviour of exploded metal cylinders and the effects of wall materials, configuration, explosive energy and initiated locations *Int. J. Impact Eng.* **35** 1578–86
[17] Shapoval A, Mos'pan D and Dragobetskii V 2016 Ensuring high performance characteristics for explosion-welded bimetals *Metallurgist* **60** 313–7
[18] Choi S J, Lee K H and Gudmestad O T 2015 The effect of dynamic amplification due to a structures vibration on breaking wave impact *Ocean Eng.* **96** 8–20

[19] Zhang A, Chen S, Wei H and Zhang X 2010 Discussion of strain rate of building structure under blasting vibration response *Blasting* **27** 9–12

[20] Chung L, Reinhorn A and Soong T 1988 Experiments on active control of seismic structures *J. Eng. Mech.* **114** 241–56

[21] Gates W E and Morden M 1996 Professional structural engineering experience related to welded steel moment frames following the Northridge earthquake *Struct. Des. Tall Build.* **5** 29–44

[22] Gertsch R, Gertsch L and Rostami J 2007 Disc cutting tests in Colorado Red Granite: implications for TBM performance prediction *Int. J. Rock Mech. Min. Sci.* **44** 238–46

[23] Balci C 2009 Correlation of rock cutting tests with field performance of a TBM in a highly fractured rock formation: a case study in Kozyatagi-Kadikoy metro tunnel, Turkey *Tunnelling Underground Space Technol.* **24** 423–35

[24] Gao S, Kang R, Dong Z and Zhang B 2013 Edge chipping of silicon wafers in diamond grinding *Int. J. Mach. Tools Manuf.* **64** 31–7

[25] Molinari A, Soldani X and Miguélez M 2013 Adiabatic shear banding and scaling laws in chip formation with application to cutting of Ti-6Al-4V *J. Mech. Phys. Solids* **61** 2331–59

[26] Lorentzon J, Järvstråt N and Josefson B 2009 Modelling chip formation of alloy 718 *J. Mater. Process. Technol.* **209** 4645–53

[27] Wang B, Liu Z and Yang Q 2013 Investigations of yield stress, fracture toughness, and energy distribution in high speed orthogonal cutting *Int. J. Mach. Tools Manuf.* **73** 1–8

[28] Schulz H, Abele E and Sahm A 2001 Material aspects of chip formation in HSC machining *CIRP Ann.* **50** 45–8

[29] Sutter G and List G 2013 Very high speed cutting of Ti-6Al-4V titanium alloy-change in morphology and mechanism of chip formation *Int. J. Mach. Tools Manuf.* **66** 37–43

[30] Zhang B and Howes T D 1995 Subsurface evaluation of ground ceramics *CIRP Ann.* **44** 263–6

[31] Zhou L, Shimizu J, Muroya A and Eda H 2003 Material removal mechanism beyond plastic wave propagation rate *Precis. Eng.* **27** 109–16

[32] Masuda K, Mizutani H and Yamada I 1987 Experimental study of strain-rate dependence and pressure dependence of failure properties of granite *J. Phys. Earth* **35** 37–66

[33] Zhang Q B and Zhao J 2014 A review of dynamic experimental techniques and mechanical behaviour of rock materials *Rock Mech. Rock Eng.* **47** 1411–78

[34] Frew D J, Forrestal M J and Chen W 2002 Pulse shaping techniques for testing brittle materials with a split hopkinson pressure bar *Exp. Mech.* **42** 93–106

[35] Liu W D, Liu K X and Xia X X 2010 The failure stress of bulk metallic glasses under very high strain-rate *J. Mater. Res.* **25** 1230–4

[36] Liu W D and Liu K X 2010 Mechanical behavior of a Zr-based metallic glass at elevated temperature under high strain-rate *J. Appl. Phys.* **108** 033511

[37] Meyers M, Xu Y, Xue Q, Pérez-Prado M T and McNelley T R 2003 Microstructural evolution in adiabatic shear localization in stainless steel *Acta Mater.* **51** 1307–25

[38] Wang B and Liu Z 2016 Investigations on deformation and fracture behavior of workpiece material during high speed machining of 7050-T7451 aluminum alloy *CIRP J. Manuf. Sci. Technol.* **14** 43–54

[39] Wang B and Liu Z 2014 Investigations on the chip formation mechanism and shear localization sensitivity of high-speed machining Ti-6Al-4V *Int. J. Adv. Manuf. Technol.* **75** 1065–76

[40] Tian L, Fu Y, Xu J, Li H and Ding W 2015 The influence of speed on material removal mechanism in high speed grinding with single grit *Int. J. Mach. Tools Manuf.* **89** 192–201

[41] Clifton R J and Klopp R W 1985 Pressure-shear plate impact testing *Met. Handbook* **8** 230–9

[42] Nicholas T 1981 Tensile testing of materials at high rates of strain *Exp. Mech.* **21** 177–85

[43] Frew D J, Akers S A, Chen W and Green M L 2010 Development of a dynamic triaxial Kolsky bar *Meas. Sci. Technol.* **21** 105704

[44] Rome J, Isaacs J and Nemat-Nasser S 2002 Hopkinson techniques for dynamic triaxial compression tests *Recent Advances in Experimental Mechanics* (Berlin: Springer) pp 3–12

[45] Xue Q, Meyers M and Nesterenko V 2002 Self-organization of shear bands in titanium and Ti-6Al-4V alloy *Acta Mater.* **50** 575–96

[46] Poulachon G, Moisan A L and Jawahir I 2007 Evaluation of chip morphology in hard turning using constitutive models and material property data *J. Manuf. Sci. Eng.* **129** 41–7

[47] Recht R F 1978 Taylor ballistic impact modelling applied to deformation and mass loss determinations *Int. J. Eng. Sci.* **16** 809–27

[48] Mondal C, Mishra B, Jena P K, Kumar K S and Bhat T B 2011 Effect of heat treatment on the behavior of an AA7055 aluminum alloy during ballistic impact *Int. J. Impact Eng.* **38** 745–54

[49] Johnson G R 1983 A constitutive model and data for materials subjected to large strains, high strain-rates, and high temperatures *Proc. 7th Inf. Symp. Ballistics* pp 541–7

[50] Calamaz M, Coupard D and Girot F 2008 A new material model for 2D numerical simulation of serrated chip formation when machining titanium alloy Ti-6Al-4V *Int. J. Mach. Tools Manuf.* **48** 275–88

[51] Pan Z, Shih D S, Tavei A, Garmestani H and Liang S Y 2017 Modeling of Ti-6Al-4V machining force considering material microstructure evolution *Int. J. Adv. Manuf. Technol.* **91** 2673–80

[52] Rule W K and Jones S 1998 A revised form for the Johnson–Cook strength model *Int. J. Impact Eng.* **21** 609–24

[53] Li G 2009 Prediction of adiabatic shear in high-speed machining based on linear perturbation analysis *Doctoral Dissertation* Dalian University of Technology

[54] Wang X, Huang C, Zou B, Liu H, Zhu H and Wang J 2013 Dynamic behavior and a modified Johnson–Cook constitutive model of Inconel 718 at high strain-rate and elevated temperature *Mater. Sci. Eng.* A **580** 385–90

[55] Lin Y, Chen X M and Liu G 2010 A modified Johnson–Cook model for tensile behaviors of typical high-strength alloy steel *Mater. Sci. Eng.* A **527** 6980–6

[56] Holmquist T J and Johnson G R 2011 A computational constitutive model for glass subjected to large strains, high strain-rates and high pressures *J. Appl. Mech.* **78** 051003

[57] Johnson G R and Holmquist T J 1994 An improved computational constitutive model for brittle materials *AIP Conf. Proc.* **309** 981–4

[58] Lv G 2017 Computer simulation of the effect of copper-riched precipitates on hardening and embrittlement in reactor pressure vessel steels *Doctoral Dissertation* University of Science and Technology Beijing

[59] Follansbee P and Kocks U 1988 A constitutive description of the deformation of copper based on the use of the mechanical threshold stress as an internal state variable *Acta Metall.* **36** 81–93

[60] Meyers M A, Benson D J, Vöhringer O, Kad B K, Xue Q and Fu H-H 2002 Constitutive description of dynamic deformation: physically-based mechanisms *Mater. Sci. Eng.* A **322** 194–216

[61] MF A 1975 Thermodynamics and kinetics of slip *Prog. Mater. Sci.* **19** 1–281

[62] Clifton R 1971 Analysis of elastic-visco-plastic waves of finite uniaxial strain *Report* MSL-70-32

[63] Zerilli F J and Armstrong R W 1987 Dislocation-mechanics-based constitutive relations for material dynamics calculations *J. Appl. Phys.* **61** 1816–25

[64] Mecking H and Kocks U 1981 Kinetics of flow and strain-hardening *Acta Metall.* **29** 1865–75

[65] Steinberg D and Lund C 1989 A constitutive model for strain rates from 10^{-4} to 10^{6} s^{-1} *J. Appl. Phys.* **65** 1528–33

[66] Wedberg D and Lindgren L E 2015 Modelling flow stress of AISI 316L at high strain-rates *Mech. Mater.* **91** 194–207

[67] Gao C and Zhang L 2012 Constitutive modelling of plasticity of fcc metals under extremely high strain-rates *Int. J. Plast.* **32** 121–33

[68] Galligan J M, McKrell T J and Robson M T 2000 Dislocation drag processes *Mater. Sci. Eng.* A **287** 259–64

[69] Tang Y 2018 Uncovering the inertia of dislocation motion and negative mechanical response in crystals *Sci. Rep.* **8** 140

[70] Regazzoni G, Kocks U F and Follansbee P S 1987 Dislocation kinetics at high strain-rates *Acta Metall.* **35** 2865–75

[71] Mao Z N, An X H, Liao X Z and Wang J T 2018 Opposite grain size dependence of strain rate sensitivity of copper at low vs high strain-rates *Mater. Sci. Eng.* A **738** 430–8

[72] Wang Q and Liu Z 2018 Microhardness prediction based on a microstructure-sensitive flow stress model during high speed machining Ti-6Al-4V *J. Manuf. Sci. Eng.* **140** 091003

[73] Outeiro J, Umbrello D and M'saoubi R 2006 Experimental and numerical modelling of the residual stresses induced in orthogonal cutting of AISI 316L steel *Int. J. Mach. Tools Manuf.* **46** 1786–94

[74] Johnson G R, Hoegfeldt J, Lindholm U and Nagy A 1983 Response of various metals to large torsional strains over a large range of strain rates-Part 1: ductile metals *J. Eng. Mater. Technol.* **105** 42–7

[75] Chiem C and Duffy J 1983 Strain rate history effects and observations of dislocation substructure in aluminum single crystals following dynamic deformation *Mater. Sci. Eng.* **57** 233–47

[76] Bleck W and Schael I 2000 Determination of crash-relevant material parameters by dynamic tensile tests *Steel Res.* **71** 173–8

[77] Grässel O, Krüger L, Frommeyer G and Meyer L 2000 High strength Fe-Mn-(Al, Si) TRIP/TWIP steels development-properties-application *Int. J. Plast.* **16** 1391–409

[78] Boyce B L and Dilmore M F 2009 The dynamic tensile behavior of tough, ultrahigh-strength steels at strain-rates from 0.0002 s^{-1} to 200 s^{-1} *Int. J. Impact Eng.* **36** 263–71

[79] Kim J H, Kim D, Han H N and Barlat F 2013 Strain rate dependent tensile behavior of advanced high strength steels: Experiment and constitutive modeling *Mater. Sci. Eng.* A **559** 222–31

[80] Liu X 2010 Dynamic constitutive relationship of TC4 titanium alloy *Doctoral Dissertation* Nanjing University of Aeronautics and Astronautics

[81] Bhat H S, Rosakis A J and Sammis C G 2012 A micromechanics based constitutive model for brittle failure at high strain-rates *J. Appl. Mech.* **79** 031016

[82] Rosakis A J and Zehnder A T 1985 On the dynamic fracture of structural metals *Int. J. Fract.* **27** 169–86

[83] Deng X and Rosakis A J 1991 Dynamic crack propagation in elastic-perfectly plastic solids under plane stress conditions *J. Mech. Phys. Solids* **39** 683–722

[84] Li X, Li H, Zhang Q B, Liang J L and Zhao J 2018 Dynamic fragmentation of rock material: Characteristic size, fragment distribution and pulverization law *Eng. Fract. Mech.* **199** 739–59

[85] Zakir S M, Zhen W, Tao S, Yulong L, Fenghua Z, Sohail A and Dar U A 2018 High rate response and dynamic failure of aluminosilicate glass under compression loading *Proc. Struct. Integrity* **13** 1244–9

[86] Grady D and Kipp M 1985 Mechanisms of dynamic fragmentation: factors governing fragment size *Mech. Mater.* **4** 311–20

[87] Clifton R J 2000 Response of materials under dynamic loading *Int. J. Solids Struct.* **37** 105–13

[88] Nieh T G and Wadsworth J 2006 Homogeneous deformation of bulk metallic glasses *Scr. Mater.* **54** 387–92

[89] Lu J, Ravichandran G and Johnson W L 2003 Deformation behavior of the Zr41.2Ti13.8Cu12.5Ni10Be22.5 bulk metallic glass over a wide range of strain-rates and temperatures *Acta Mater.* **51** 3429–43

[90] Yu H B, Shen X, Wang Z, Gu L, Wang W H and Bai H Y 2012 Tensile plasticity in metallic glasses with pronounced β relaxations *Phys. Rev. Lett.* **108** 015504

[91] Turley D M, Doyle E D and Ramalingam S 1982 Calculation of shear strains in chip formation in titanium *Mater. Sci. Eng.* **55** 45–8

[92] Shaw M C and Cookson J 2005 *Metal Cutting Principles* (New York: Oxford University Press)

[93] Wright T W and Ockendon H 1996 A scaling law for the effect of inertia on the formation of adiabatic shear bands *Int. J. Plast.* **12** 927–34

[94] Wang B, Liu Z, Song Q, Wan Y and Shi Z 2016 Proper selection of cutting parameters and cutting tool angle to lower the specific cutting energy during high speed machining of 7050-T7451 aluminum alloy *J. Clean. Prod.* **129** 292–304

[95] Ma W, Chen X and Shuang F 2017 The chip-flow behaviors and formation mechanisms in the orthogonal cutting process of Ti-6Al-4V alloy *J. Mech. Phys. Solids* **98** 245–70

[96] Ye G, Xue S, Ma W and Dai L 2017 Onset and evolution of discontinuously segmented chip flow in ultra-high-speed cutting Ti-6Al-4V *Int. J. Adv. Manuf. Technol.* **88** 1161–74

[97] Zhao D, Sangesland S and Vedvik N 2016 An experimental study of axial vibration assisted drilling *J. Nat. Gas Sci. Eng.* **35** 1158–66

[98] Lv D, Huang Y, Wang H, Tang Y and Wu X 2013 Improvement effects of vibration on cutting force in rotary ultrasonic machining of BK7 glass *J. Mater. Process. Technol.* **213** 1548–57

[99] Wang J, Zhang C, Feng P and Zhang J 2016 A model for prediction of subsurface damage in rotary ultrasonic face milling of optical K9 glass *Int. J. Adv. Manuf. Technol.* **83** 347–55

[100] Kahraman S 2002 Correlation of TBM and drilling machine performances with rock brittleness *Eng. Geol.* **65** 269–83

[101] Gong Q M and Zhao J 2007 Influence of rock brittleness on TBM penetration rate in Singapore granite *Tunnelling Underground Space Technol.* **22** 317–24

[102] Wu W R, Lou L and Liang X J 2017 Cutting features of damage rock by shock disturbance *J. Cent. South Univ. (Sci. Technol.)* **48** 2709–14

[103] Zhang Y Q, Lu Y and Hao H 2004 Analysis of fragment size and ejection velocity at high strain-rate *Int. J. Mech. Sci.* **46** 27–34

[104] Kipp M and Grady D 1985 Dynamic fracture growth and interaction in one dimension *J. Mech. Phys. Solids* **33** 399–415

[105] Zhang W, Zhang Y and Zhang G 2011 Single and multiple dynamic impacts behaviour of ultra-high performance cementitious composite *J. Wuhan Univ. Technol.—Mater. Sci. Ed.* **26** 1227–34

[106] Von Karman T and Duwez P 1950 The propagation of plastic deformation in solids *J. Appl. Phys.* **21** 987–94

[107] Wang L 2011 *Foundations of Stress Waves* (Amsterdam: Elsevier)

[108] Jiang F, Li Z M, Wang N C, Guo H and Xu X P 2016 Research on dynamic characteristics of Shanxi black granite under high strain-rates *J. Vib. Shock* **35** 177–82
[109] Huang S, Xia K and Zheng H 2013 Observation of microscopic damage accumulation in brittle solids subjected to dynamic compressive loading *Rev. Sci. Instrum.* **84** 093903
[110] Liu J, Fan Q, Cai H and Wang F 2015 Underlying mechanism of periodical adiabatic shear bands generated in Ti-6Al-4V target by projectile impact *Mater. Des.* **87** 231–7
[111] Zheng C *et al* 2015 Failure mechanisms in ballistic performance of Ti-6Al-4V targets having equiaxed and lamellar microstructures *Int. J. Impact Eng.* **85** 161–9
[112] Rice J R and Thomson R 1974 Ductile versus brittle behaviour of crystals *Phil. Mag.: J. Theor. Exp. Appl. Phys.* **29** 73–97
[113] Wang B, Liu Z, Su G and Ai X 2015 Brittle removal mechanism of ductile materials with ultrahigh-speed machining *J. Manuf. Sci. Eng.* **137** 061002
[114] Lawn B and Wilshaw T R 1993 *Fracture of Brittle Solids* (Cambridge: Cambridge University Press)
[115] Armstrong R and Walley S 2008 High strain-rate properties of metals and alloys *Int. Mater. Rev.* **53** 105–28
[116] Mahalingam S, Flewitt P and Knott J 2013 The ductile-brittle transition for nominally pure polycrystalline nickel *Mater. Sci. Eng.* A **564** 342–50
[117] Abushawashi Y, Xiao X and Astakhov V 2011 Modeling of serrated chip formation with a fracture locus approach *Proc. ASME 2011 Int. Mechanical Engineering Congress and Exposition* (American Society of Mechanical Engineers) pp 373–84
[118] Griffith A A 1921 The phenomena of rupture and flow in solids *Phil. Trans. R. Soc.* A **221** 163–98
[119] Orowan E 1949 Fracture and strength of solids *Rep. Prog. Phys.* **12** 185
[120] Stroh A 1954 The formation of cracks as a result of plastic flow *Proc. R. Soc.* A **223** 404–14
[121] Cottrell A H 1958 Theory of brittle fracture in steel and similar metals *Trans. Met. Soc. AIME* **212**
[122] Li H, Fan C, Tao K, Choo H and Liaw P K 2006 Compressive behavior of a Zr-based metallic glass at cryogenic temperatures *Adv. Mater.* **18** 752–4
[123] Qiao J C, Wang Q and Pelletier J M 2019 Structural heterogeneities and mechanical behavior of amorphous alloys *Prog. Mater. Sci.* **104** 250–329
[124] Donovan P E and Stobbs W M 1981 The structure of shear bands in metallic glasses *Acta Metall.* **29** 1419–36
[125] Argon A S 1979 Plastic deformation in metallic glasses *Acta Metall.* **27** 47–58
[126] Chen H, He Y, Shiflet G J and Poon S J 1994 Deformation-induced nanocrystal formation in shear bands of amorphous alloys *Nature* **367** 541–3
[127] Zhang B and Yin J 2019 The 'skin effect' of subsurface damage distribution in materials subjected to high-speed machining *Int. J. Extreme Manuf.* **1** 012007
[128] Jones R E 1973 Fatigue crack growth retardation after single-cycle peak overload in Ti-6Al-4V titanium alloy *Eng. Fract. Mech.* **5** 585–604
[129] Krishnan K, Sockalingam S, Bansal S and Rajan S D 2010 Numerical simulation of ceramic composite armor subjected to ballistic impact *Composites* B **41** 583–93
[130] Crouch I G, Kesharaju M and Nagarajah R 2015 Characterisation, significance and detection of manufacturing defects in reaction sintered silicon carbide armour materials *Ceram. Int.* **41** 11581–91
[131] Lundberg P 2004 Interface defeat and penetration: two modes of interaction between metallic projectiles and ceramic targets *Doctoral Dissertation* Acta Universitatis Upsaliensis
[132] Salomon C 1931 Process for the machining of metals of similarly-acting materials when being worked by cutting tools *German Patent* 523594